

# Holographic Measurements of Anisotropic Three-Dimensional Diffusion of Colloidal Clusters

# SUPPLEMENTARY INFORMATION FOR "HOLOGRAPHIC MEASUREMENTS OF ANISOTROPIC THREE-DIMENSIONAL DIFFUSION OF COLLOIDAL CLUSTERS"

JEROME FUNG AND VINOTHAN N. MANOHARAN

## 1. Hologram Analysis and Data Reduction

We describe in further detail how we fit scattering models to the holograms we record of dimers and trimers to extract 3D dynamical information, with attention to issues that arise with the large number of holograms (∼20,000) we must analyze for each case.

### 1.1. Model Fitting Procedure.

Our technique of fitting scattering solutions to holograms has previously been described [1, 2]. For the dimers, we fit a scattering model that depends on one refractive index for both particles, the radius of each particle, the 3D position of the dimer center of mass, 2 orientational Euler angles, and a scaling parameter [1]. The model for trimers differs only in that we fit for three orientation angles and for only one average radius [2].

The largest bottleneck in fitting scattering models to large numbers of holograms using Levenberg-Marquardt minimizers is that an initial guess for the model parameters needs to be provided for each hologram. With time series of holograms, only one initial guess is necessary, in principle: we can use the best-fit parameters of each hologram as the initial guess for the next. We have found it effective to speed up this process by doing an initial rough fit to a randomly chosen subset of 10% of the pixels of each hologram. Subsequently, we use the parameters obtained from the rough fits as initial guesses for a fit to all the pixels. We do this second stage of fitting in parallel.

### 1.2. Validating Model Fits to Trimer Holograms.

The model for the trimer holograms has an additional orientational degree of freedom compared to the model for the dimer holograms. We have noticed that on occasion the fitter converges to best-fit parameters that result in the best-fit model hologram having subtle differences when compared to the experimental hologram; this usually stems from the orientation angles being incorrect. We do not observe this problem for the dimer holograms. To detect holograms with potentially incorrect best-fit parameters, we inspect the $R^2$ statistic [2] of the fits. We also compute a $\chi^2$ statistic for a binary version of the experimental and best-fit holograms, where all pixels above the mean of 1 are set to a value of 1 and all remaining pixels are set to a value of 0. The binary image is much more sensitive to the shape of the interference fringes.

When we compute correlation functions such as mean-squared displacements from the trimer holograms, we reject the contribution from any holograms where either $R^2$ or binary $\chi^2$ is worse than 2 standard deviations from a rolling mean. Manual inspection of 200 randomly chosen trimer holograms that were not rejected

under these criteria revealed 7 questionable fits. We infer from the Poisson distribution that, to a 99% confidence level, the percentage of remaining bad fits is less than 8%. We also reject the contribution from a given pair of holograms if the probability of obtaining either a center of mass displacement or angular displacement of the observed magnitude is less than $10^{-5}$. We compute these probabilities using estimates for the diffusion tensor elements, and choose the threshold of $10^{-5}$ to avoid biasing the observed distribution and to make the cutoffs weakly sensitive to the estimates for $\mathbf{D}$.

Performing this cutoff procedure requires knowing the probability distributions governing translational and rotational displacements. The probability distribution for translational displacements is Gaussian, but the distribution function for rotational displacements is not. Instead, the probability density function $f_i(\theta;\tau)$ for observing an angle $\theta$ between cluster axis $\mathbf{u}_i(t)$ at a given time $t$ and after a time interval $\tau$ is given by

$$f_i(\theta;\tau) = \sum_{\ell=0}^{\infty} Y_\ell^0(0) Y_\ell^0(\theta) \exp\left[-\ell(\ell+1) D_{r,\text{eff}} \tau\right] \tag{S1}$$

where $D_{r,\text{eff}} = (D_{r,j} + D_{r,k})/2$, $D_{r,j}$ and $D_{r,k}$ are the elements of $\mathbf{D}^{rr}$ describing rotations about the two cluster axes other than $i$, and $Y_\ell^0(\theta)$ denote spherical harmonics with $m = 0$. We briefly discuss the origin of this distribution function in Section 2.

As a final verification that our holographic imaging is correct and that any remaining errors do not substantially affect the dynamics we measure, we compute probability distribution functions for the dynamical quantities we use to measure $\mathbf{D}$ from the data. Figure S1 shows a representative sample for several lag times $\tau$. We first examine the cosine of the angle traversed by $\mathbf{u}_3$, or $\mathbf{u}_3(t) \cdot \mathbf{u}_3(t+\tau)$, in Figure S1(a). Aside from a noise floor, we find that the measured distributions agree well with the expected distributions computed from Eq. S1 and the measured values of $\mathbf{D}^{rr}$. We observe similarly good agreement for the distributions of particle-frame displacements along axis 3 shown in Figure S1(b).

1.3. **Estimating Uncertainties in Elements of D.** The uncertainties in the elements of $\mathbf{D}$ are derived from the cluster trajectories obtained from holographic microscopy. The elements of $\mathbf{D}$ are measured by computing a correlation function (an MSD or axis autocorrelation) for a range of time steps $\tau$, and by fitting a theoretical expression involving the elements of $\mathbf{D}$ (Eqs. 1, 3, or 4 in the manuscript) to the points of the correlation function. The uncertainties we report are the appropriate diagonal elements of the covariance matrix of the best-fit parameters.

Determining the uncertainties in the elements of $\mathbf{D}$ in this manner requires the points in the correlation functions to be weighted by the uncertainty associated with each point. The uncertainty we consider is the statistical error related to the number of uncorrelated displacements that we use to calculate each point. The statistical error is directly estimated from the appropriate cluster trajectory using a block decorrelation procedure [3]. We choose the block decorrelation method because it does not require any *a priori* assumptions about the underlying statistical distribution governing the displacements.

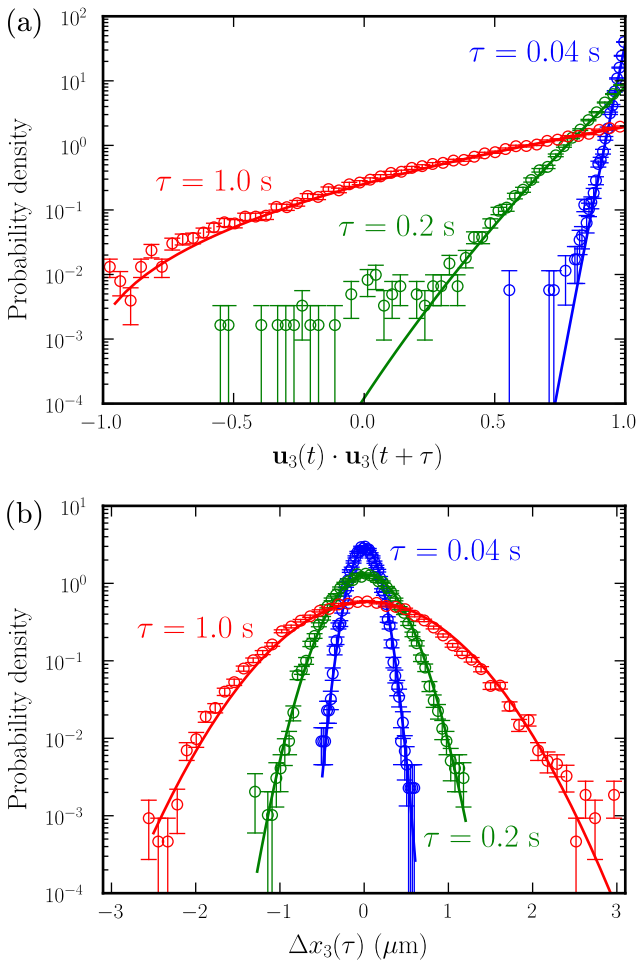


FIGURE S1. Distribution functions for trimer angular displacements and cluster-frame displacements. Histogram points computed from experimental data are shown in open symbols; solid lines show theoretical predictions computed from elements of **D** reported in Table II of the body of the paper. (a) Rotational dynamics of $\mathbf{u}_3$. Predicted distribution computed from Eq. S1. (b) Cluster-frame displacements along axis 3. Theoretical distribution is a Gaussian with a mean of 0 and a variance of $2D_{t,3}\tau$.

1.4. **Comparison to confocal microscopy.** The precision with which we measure elements of **D** consequently increases with the number of observed displacements and hence with the length of the trajectories we observe. The rapid acquisition times of holographic microscopy give it an advantage over complementary 3D imaging techniques such as confocal microscopy in that a considerably larger number of 3D images can be acquired in the same amount of experimental time.

The main advantage of holographic microscopy over confocal microscopy, however, lies in the greater sensitivity of experiments using holographic microscopy to weakly anisotropic diffusion. In confocal experiments on diffusion, the acquisition time needed to scan through a 3D volume ($\sim$ 1 s or more) requires the dynamics to be slowed down through the use of larger particles and more viscous solvents. This results in the elements of $\mathbf{D}$ being much smaller. For example, tetrahedral sphere clusters used in confocal measurements of diffusion [4] have an isotropic rotational diffusion constant of $D_r \sim 5 \times 10^{-3}$ s$^{-1}$, nearly two orders of magnitude smaller than in our trimer experiment. Consequently, given the same amount of experimental time, confocal experiments access much shorter timescales relative to the rotational diffusion times than holographic experiments. This makes it more challenging to observe statistically significant anisotropy in $\mathbf{D}$, as we now show.

Demonstrating anisotropic diffusion requires showing that the ratio of the rotational autocorrelation functions about axes $i$ and $j$ differs from 1 by a statistically significant amount. Eq. 3 of our manuscript gives this ratio in terms of the relevant elements of $\mathbf{D}$:

$$\frac{\langle \mathbf{u}_i(t) \cdot \mathbf{u}_i(t+\tau) \rangle}{\langle \mathbf{u}_j(t) \cdot \mathbf{u}_j(t+\tau) \rangle} = \exp\left[-(D_{r,j} - D_{r,i})\tau\right] \tag{S2}$$

$$\approx 1 - (D_{r,j} - D_{r,i})\tau + \ldots \tag{S3}$$

where we have assumed in the second step that the anisotropy is small. The ratio differs from 1 in proportion to the *magnitude* of the difference in the rotational diffusion constants, rather than in proportion to the relative difference. Consider a confocal experiment and a holographic experiment on systems with the same relative anisotropy $D_{r,i}/D_{r,j}$, where both experiments measure the same number of independent displacements over the same time interval $\tau$. Both experiments will compute autocorrelations at $\tau$ with the same precision and will require similar amounts of experimental time. But for the confocal experiment, $(D_{r,j} - D_{r,i})\tau$ will be smaller, and may even be comparable to the measurement precision of the autocorrelations. Thus, because holographic microscopy can study more rapidly diffusing clusters, it is easier to observe weakly anisotropic diffusion, as we show in our measurement of the the 3% difference between $D_{r,1}$ and $D_{r,2}$ for the trimer.

## 2. Probability Distribution for Rotational Displacements

We briefly describe the origin of Eq. S1, the probability density function for finite rotational displacements. As described in Section 1.2, we use this distribution to reject pairs of holograms that exhibit highly improbable angular displacements, most likely due to an incorrect model fit. Our discussion here is primarily physical and draws heavily from that of Berne & Pecora [5]; the reader interested in a more rigorous but abstract discussion is referred to [6, 7].

To calculate the relevant distribution function, we will consider what happens to an imaginary ensemble of clusters undergoing rotational diffusion. We will assume that translation-rotation coupling is negligible, so that we can consider the rotational motions independently of the translations. Suppose that we observe only the motion of one body axis $\mathbf{u}_i$ as the clusters in the ensemble undergo rotational diffusion. Lastly, suppose that that we prepare the ensemble such that at $t = 0$, $\mathbf{u}_i$ for every cluster lies at the same point on the unit sphere, which we may choose to be at $\theta = 0$ without loss of generality. We seek to compute the probability

distribution $f_i(\theta, \phi; \tau)$ such that

$$\int_{\phi_0}^{\phi_1} \int_{\theta_0}^{\theta_1} f_i(\theta, \phi; \tau) \sin\theta d\theta d\phi \tag{S4}$$

gives the probability of finding $\mathbf{u}_i$ between $\phi_0$ and $\phi_1$ and between $\theta_0$ and $\theta_1$ at $t = \tau$.

For isotropic rotational diffusion, such as that of a sphere, calculating $f_i$ is straightforward: the diffusion can be described by a rotational Fick's law characterized by a single rotational diffusion constant $D_r$ [5]. The initial condition

$$f_i(\theta, \phi; 0) = \frac{\delta(\theta)}{2\pi \sin\theta}, \tag{S5}$$

where $\delta(\theta)$ denotes the Dirac delta function, then determines $f_i(\theta, \phi; \tau)$. This idea can be generalized to the case we are interested in, where $\mathbf{D}^{rr}$ is diagonal but not isotropic, using Brenner's tensorial formalism [7]. Because the details are quite involved[1], we instead give a physical argument that allows us to apply the isotropic solution to the anisotropic case.

The time evolution of $f_i$ must be governed by $D_{r,j}$ and $D_{r,k}$, the diffusion constants for rotations about the other two cluster axes. In our ensemble of clusters, prepared such that all clusters initially have $\mathbf{u}_i$ at $\theta = 0$, the clusters will not all have the same orientation: $\mathbf{u}_j$ and $\mathbf{u}_k$ can lie anywhere on the equator of the unit sphere. Consequently, observing only the motion of $\mathbf{u}_i$, we will on average observe $f_i$ evolving according to an effective rotational diffusion constant $D_{r,\text{eff}}$ where $D_{r,\text{eff}} = (D_{r,j} + D_{r,k})/2$. We may then straightforwardly adopt the result from isotropic diffusion [5], which leads to Eq. S1. Note that $f_i$ is ultimately independent of $\phi$ because of the symmetric manner in which we prepared the ensemble.

## 3. Estimating Solvent Viscosities

Here we discuss in greater detail the inference of the solvent viscosities $\eta$ needed to compare experimentally measured elements of the diffusion tensor $\mathbf{D}$ to theoretical predictions.

The viscosity of our solvent, a mixture of $H_2O$ and $D_2O$ chosen to density-match polystyrene particles, has a strong temperature dependence. Figure S2 shows that the viscosity of a bulk sample of the solvent, measured using a Cannon-Manning capillary viscometer, varies by nearly 20% over a 6°C temperature range. We performed all the experiments described in the body of the paper at room temperature, but we have observed that the room temperature can change by several °C over the course of a few hours, most likely due to the cycling of the building heating and air conditioning systems. Moreover, particularly if the laboratory room temperature is changing, the temperature in the sample, sealed in a glass sample cell, may differ from that of the surrounding air.

Consequently, we believe that that the best way to estimate the solvent viscosity is to observe the *in situ* diffusion of single colloidal spheres, which are always present in the sample due to the arrested aggregation technique we use to make the clusters, either immediately before or immediately after imaging the diffusion of a cluster of

[1]Displacements of the 3 orientational generalized coordinates $q^i$ in Brenner's formalism cannot describe non-infinitesimal rotations. To describe finite rotations, it is necessary to adopt a formalism such as Euler angles; see Sec. IX of Brenner's paper for details. The general case may also be handled by coordinate-free operator methods [6].

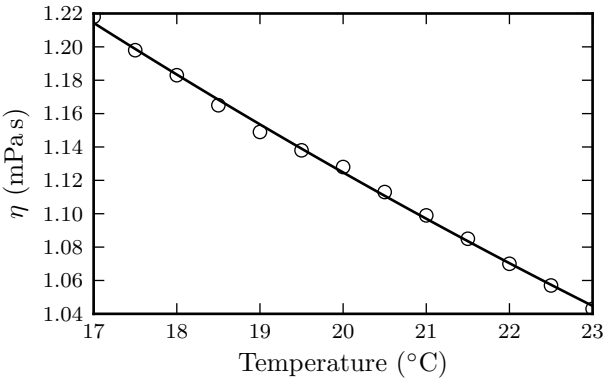


FIGURE S2. Temperature dependence of solvent viscosity. Data points, open symbols, were measured with a Cannon-Manning capillary viscometer. The solid line is a best-fit quadratic function that allows for interpolation between the measured points. Ambient laboratory temperatures in the diffusion experiments varied from 19–23 °C.

interest. The Stokes-Einstein relation gives the translational diffusion constant[2] $D$ in terms of the temperature $T$, the particle radius $a$, and the solvent viscosity $\eta$:

$$D = \frac{k_B T}{6\pi\eta a}. \tag{S6}$$

Using Eq. S6, once we determine $D$ for a diffusing sphere of radius $a$, we can infer the ratio $k_BT/\eta$. Because of the strong temperature dependence illustrated in Figure S2, $k_BT$ and $\eta$ should not be viewed as independent parameters. Moreover, from dimensional considerations, the elements of $\mathbf{D}$ are always proportional to $k_BT/\eta$. Once we determine $k_BT/\eta$, we use the best-fit line to the data in Figure S2 to infer $\eta$ and $k_BT$ separately. While this is not the usual context in which microrheological experiments are performed, we essentially treat the diffusing single spheres as *in situ* thermometers.

We obtain $D$ from an MSD computed from the 3D trajectory of a diffusing particle: $\langle \Delta\mathbf{r}^2(\tau)\rangle = 6D\tau$. In all cases, we obtain the trajectory using holography and record holograms at 25 frames per second. We obtain a radius, index of refraction, and 3D position from each hologram by fitting a model based on the Lorenz-Mie solution [8].

For the dimer experiment, which used particles with a nominal radius of 650 nm, we measure $D = 2.533 \pm 0.017 \times 10^{-13}$ m$^2$s$^{-1}$ for a diffusing particle with an optical radius of 639 nm. If we assume that the particle has the same enhanced hydrodynamic radius of 709 nm as we inferred from the dimer data, independent of any considerations of $k_BT$ or $\eta$, we can subsequently use the data in Figure S2 to infer a solvent viscosity of 1.187 mPa s, which is within 3% of the best-fit solvent viscosity, 1.159 mPa s. The consistency of these values, along with the

[2]In terms of the diffusion tensor $\mathbf{D}$, for a sphere $\mathbf{D}$ is diagonal, and $\mathbf{D}^{tt} = D\mathbf{I}$, where $\mathbf{I}$ is the identity tensor.

excellent agreement between the measured and predicted values of $D_\parallel/D_\perp$, which is independent of $a$ and $k_BT/\eta$, validates our dimer measurements.

For the trimer experiment, we measured $D = 3.996 \pm 0.055 \times 10^{-13}$ m$^2$s$^{-1}$ for a diffusing sphere of nominal radius 500 nm. With no analytical theory as we had for dimers, we cannot rigorously find a best-fit radius for the trimer. We take the optical radius of the particle, 517 nm, as an estimate of the particle size and use the data in Figure S2 to infer $\eta = 1.049$ mPa s, the value we use in the HYDROSUB calculations.

## References


[1] J. Fung, K. E. Martin, R. W. Perry, D. M. Kaz, R. McGorty, and V. N. Manoharan, Opt. Express **19**, 8051 (2011).

[2] J. Fung, R. W. Perry, T. G. Dimiduk, and V. N. Manoharan, J. Quant. Spectrosc. Radiat. Transfer **113**, 2482 (2012).

[3] H. Flyvbjerg and H. G. Petersen, J. Chem. Phys. **91**, 461 (1989).

[4] G. L. Hunter, K. V. Edmond, M. T. Elsesser, and E. R. Weeks, Opt. Express **19**, 17189 (2011).

[5] B. J. Berne and R. Pecora, *Dynamic Light Scattering: With Applications to Chemistry, Biology, and Physics* (Wiley, 1976).

[6] L. D. Favro, Phys. Rev. **119**, 53 (1960).

[7] H. Brenner, J. Colloid Interface Sci. **23**, 407 (1967).

[8] S.-H. Lee, Y. Roichman, G.-R. Yi, S.-H. Kim, S.-M. Yang, A. van Blaaderen, P. van Oostrum, and D. G. Grier, Opt. Express **15**, 18275 (2007).